



Multiple drivers of production and particle export in the western tropical North Atlantic

Laura F. Korte ,¹ Geert-Jan A. Brummer ,^{1,2} Michèle van der Does ,^{1,a} Catarina V. Guerreiro ,^{3,b} Furu Mienis ,¹ Chris I. Munday,^{1,c} Leandro Ponsoni ,^{1,4} Stefan Schouten ,^{5,6} Jan-Berend W. Stuut ,^{1,2,7*}

¹NIOZ Royal Netherlands Institute for Sea Research, Department of Ocean Systems, Utrecht University, Texel, The Netherlands

²Faculty of Earth and Life Sciences, Vrije Universiteit Amsterdam, Amsterdam, The Netherlands

³Faculty of Earth Sciences, University of Bremen, Bremen, Germany

⁴Centre for Earth and Climate Research, Earth and Life Institute, Université Catholique de Louvain, Louvain-la-Neuve, Belgium

⁵NIOZ Royal Netherlands Institute for Sea Research, Department of Marine Microbiology and Biogeochemistry, Utrecht University, Texel, The Netherlands

⁶Department of Earth Science, Faculty of Geoscience, Utrecht University, Utrecht, The Netherlands

⁷MARUM Center for Marine Environmental Sciences, University of Bremen, Bremen, Germany

Abstract

To assess the impacts of Amazon River discharge, Saharan dust deposition, N₂-fixation and mixed-layer deepening on the biological carbon pump, sediment traps were moored from October 2012 to November 2013 at two sites in the western tropical North Atlantic (49°W,12°N/57°W,12°N). Particle exports interpreted along with satellite- and Argo-float data show peak fluxes in biogenic silica (31 mg m⁻² d⁻¹) and organic carbon (25 mg m⁻² d⁻¹) during the fall of 2013 that were ten to five times higher than any time earlier during the year. These high export fluxes occurred in tandem with high surface chlorophyll *a* concentrations associated with the dispersal of the Amazon River plume, following retroflection into the North-Atlantic-Counter-Current. High fucoxanthin fluxes (> 80 μg m⁻² d⁻¹) and low δ¹⁵N-values (−0.6‰) suggest a large contribution by marine diatom-diazotrophic-associations, possibly enhanced by wet Saharan dust deposition. During summer, the Amazon River plume resulted in high mass fluxes at 57°W that were enriched in biogenic silica but weakly influenced by diazotrophic-associations compared to the fall event at 49°W. High carbonate-carbon fluxes (17 mg m⁻² d⁻¹) dominated a second single event at 49°W during spring that was likely triggered by mixed-layer deepening. Rain-ratios of BSi/C_{carb} amounted to 1.7 when associated with high export fluxes linked to the Amazon River plume. Compared to an annual average of 0.3, this indicates a more efficient uptake of CO₂ via the biological pump compared to when the plume was absent, hence supporting earlier observations that the Amazon River plume is important for ocean CO₂ sequestration.

The tropical oceans are a source for natural CO₂ outgassing due to upwelling of CO₂-rich deep waters (Lefèvre et al. 1998; Takahashi et al. 2002; Mikaloff Fletcher et al. 2007). In the

tropical Atlantic, approximately 0.10–0.15 Pg of carbon are released between 14°N and 14°S on an annual basis (Takahashi et al. 2002, 2009). Regionally and seasonally, the air-sea exchange of CO₂ differs (Mikaloff Fletcher et al. 2007), within the western tropical North Atlantic (WTNA) where the biological uptake of CO₂ actually counteracts the outgassing due to seasonally enhanced primary production (Cooley and Yager 2006; Cooley et al. 2007). Of particular importance are the regions influenced by large volumes of fresh- and nutrient enriched waters provided by the Amazon River plume to the otherwise oligotrophic open ocean (Muller-Karger et al. 1988; TERNON et al. 2000; Masson and Delecluse 2001; Körtzinger 2003; Subramaniam et al. 2008). Around 175,000 m³ of fresh-water is discharged into the equatorial region at 50°W every second (Gupta 2008) and the spreading river plume impacts

*Correspondence: Jan-Berend.Stuut@nioz.nl

This is an open access article under the terms of the Creative Commons Attribution License, which permits use, distribution and reproduction in any medium, provided the original work is properly cited.

Additional Supporting Information may be found in the online version of this article.

^aPresent address: Alfred-Wegener-Institute, Helmholtz Centre for Polar and Marine Research, Bremerhaven, Germany

^bPresent address: MARE (Marine and Environmental Science Centre), Coimbra, Portugal

^cPresent address: University of Western Ontario, London, Ontario, Canada

oceanic waters far away from the river mouth (Subramaniam et al. 2008; Yeung et al. 2012; Chong et al. 2014). The distribution of the plume is strongly seasonal (Muller-Karger et al. 1988; Masson and Delecluse 2001), covering an area of around 2 million km² following dispersal by ocean currents (Körtzinger 2003). As it spreads offshore, the plume water mixes with oceanic water into a shallow surface layer with low salinity and high dissolved silicon concentrations (Shipe et al. 2006), likely also to act as a source of labile iron that was not precipitated in the Amazon estuary (Subramaniam et al. 2008). Indeed, (Guerreiro et al. 2017) have recently shown that the Amazon River plume can seasonally promote opportunistic phytoplankton groups in the surface ocean in the WTNA, including diatoms and particular fast-blooming coccolithophore species.

In addition to the Amazon River plume, the oligotrophic waters in the WTNA are also influenced by deposition of African mineral dust. Large amounts of dust particles emitted from the Sahara desert (Yu et al. 2015a) are blown across the Atlantic Ocean, reaching the Americas and the Caribbean (e.g., Prospero et al. 1970; Prospero 1999; Prospero et al. 2014). Along with the seasonal movement of the Intertropical Convergence Zone (Adams et al. 2012; Basha et al. 2015), the dust is transported by the easterly trade winds towards North America and the Caribbean Sea during summer and fall, and by the northeasterly trade winds towards the Amazon River basin during winter and spring (Prospero et al. 2014). Recent satellite observations point to ca. 182 Tg of Saharan dust leaving the African coast every year at 15°W, of which only 43 Tg reaches 75°W (Yu et al. 2015a), and 28 Tg year⁻¹ being eventually deposited into the Amazon River basin (Yu et al. 2015b). Such dust carries important macro- and micronutrients that act as fertilizers not only in the rainforest within the Amazon River basin (Yu et al. 2015b), but also across the vast North Atlantic (Jickells 1999; Gao et al. 2003) where it stimulates N₂ fixation by marine diazotrophs (Mills et al. 2004) and acts as mineral ballast for marine snow (Fischer et al. 2007; Van der Jagt et al. 2018). Saharan dust is delivered to the surface ocean via dry or wet deposition (Duce et al. 1991; Schulz et al. 2012), with the latter dominating with increasing distance from the source regions (Zhao et al. 2003) and therefore of particular relevance for the WTNA. Wet dust deposition is thought to have a greater effect on primary production and chlorophyll *a* (Chl *a*) concentrations due to prolonged cloud chemical processes and mixing with acid aerosols in the course of atmospheric transport, responsible for increasing the solubility (i.e., bioavailability) of dust-born nutrients (Ridame et al. 2014). This is especially the case for the dust-born iron, an essential element for Chl *a* synthesis and N₂ fixation by marine phytoplankton (Falkowski 1997; Carpenter et al. 1999; Mahaffey et al. 2003; Mills et al. 2004).

Nitrogen fixation by diazotrophic cyanobacteria (Carpenter et al. 1999) is responsible for reducing gaseous N₂ into more

readily bioavailable species of nitrogen (Sohm et al. 2011), while lowering the nitrogen isotope values compared to the assimilation of, e.g., nitrate (Montoya et al. 2002). The most common diazotrophic N₂ fixers in the oligotrophic open ocean are the free-living cyanobacteria *Trichodesmium*, which abound in the WTNA (Carpenter et al. 1999; Pabortsava et al. 2017), and the endosymbiont *Richelia intracellularis* living in symbiosis with diatom species such as *Hemiaulus haukii* and *Rhizolenia clevei* (Carpenter et al. 1999; Cooley and Yager 2006; Subramaniam et al. 2008; Goes et al. 2014). Combined, the latter organisms form diatom diazotrophic associations, or so-called DDAs (Subramaniam et al. 2008; Goes et al. 2014), responsible for contributing to the carbon sink of the WTNA with about 1.7 Tmol yr⁻¹ (Subramaniam et al. 2008; Yeung et al. 2012). The gravitational settling and export of such biologically-produced carbon-rich material from the surface towards the deep ocean is known as the “biological carbon pump,” influencing atmospheric CO₂ levels (Falkowski et al. 1998). The efficiency of the pump is intensified when the downward flux of organic carbon is ballasted by minerals, such as biogenic carbonate produced by coccolithophores and biogenic silica produced by diatoms, as well as by lithogenic minerals from atmospheric dust (Logan and Hunt 1987; Ittekkot 1993; Armstrong et al. 2001; Francois et al. 2002; Klaas and Archer 2002; Fischer and Karakas 2009). Such enhanced particle fluxes were earlier captured by a deep sediment trap off the west coast of Barbados, which occurred under the combined influence of Amazon River plume and Saharan dust deposition (Deuser et al. 1988).

Saharan dust deposition and the influence of the Amazon River were also observed by Guerreiro et al. (2017) and (Korte et al. 2017) although the relative importance of the underlying processes remains to be resolved. To evaluate the processes impacting the biological pump in the WTNA, we combine particle exports with in-situ depth profiling, satellite measurements and Argo float observations of relevant environmental parameters. We relate the spatial and temporal variability in mass fluxes and particle composition to the Amazon River plume, nitrogen fixation, mixed-layer deepening, and Saharan dust deposition. The occurrence of particularly high particle flux events provides crucial insights into the processes driving the biological carbon pump and hence CO₂ sequestration in the WTNA.

Material and methods

Study area and experimental setting

The WTNA is seasonally influenced by both Amazon River dispersal and by Saharan dust deposition. Both processes are strongly linked to the latitudinal migration of the Intertropical Convergence Zone (ITCZ) and have been thoroughly described in recent studies (Van der Does et al. 2016; Guerreiro et al. 2017; Korte et al. 2017; Guerreiro et al.

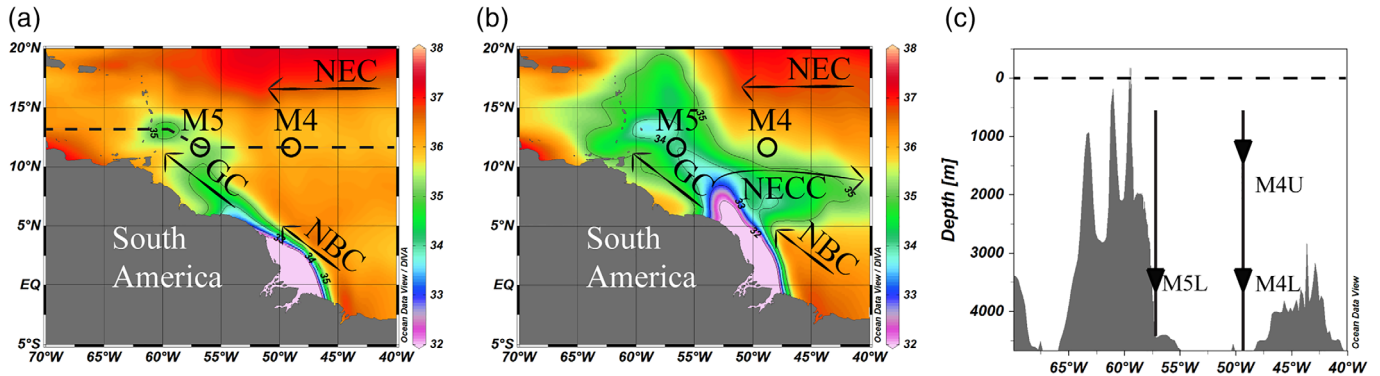


Fig. 1. Overview of the study area in the WTNA. Amazon River plume dispersal illustrated by sea surface salinity (SSS) during winter-spring (a), and summer-fall (b). SSS data were obtained for the time period of February 2013–January 2014 from Aquarius (monthly temporal resolution, 1° spatial resolution) downloaded from Giovanni of the Goddard Earth Sciences Data and Information Service Center (GES DISC) provided by NASA (disc.sci.gsfc.nasa.gov). Arrows indicate the North Equatorial Current (NEC), North Equatorial Counter Current (NECC), Guiana Current (GC), and North Brazil Current (NBC). Circles indicate the location of the moorings M4 and M5. The bathymetric profile is displayed in (c) drawn along the dashed line indicated in (a).

2019). In short, the surface water circulation in the WTNA is characterized by the North Equatorial Current (NEC) flowing westward between 7° and 20°N , as well as the North Equatorial Counter Current (NECC) flowing eastward, south of the NEC (Fig. 1a,b). The NECC intensifies approximately between 5° and 10°N during summer and fall with the northward movement of the ITCZ (Longhurst 1993; Bourlès et al. 1999). During this period, the northwest flowing North Brazil Current (NBC) is retroflected off the Brazilian coast after crossing the equator and fed into the NECC (Muller-Karger et al. 1988). As seen from remote sensing ocean color measurements, occasionally rings are formed outgoing from the NBC propagating towards the northwest (Fratantoni and Glickson 2001). In winter, when the ITCZ is moving towards the south, the trade winds weaken, resulting in the attenuation of the NECC. During this time, both the NBC and Amazon River plume are not retroflected but rather flow in northwestward direction along the northeastern South American coast feeding the Guiana Current (GC) (Masson and Delecluse 2001).

The sediment traps were attached to two long-term moorings along the 12°N parallel at 49°W and 57°W (M4 and M5, respectively; Fig. 1, Table 1). While site M5 was more likely under the influence of the Amazon River dispersal throughout the year, site M4 was located in a more oligotrophic open ocean setting. Both moorings were situated underneath the core of the largest Saharan dust plume crossing the Atlantic Ocean (Adams et al. 2012; Prospero et al. 2014; Yu et al. 2015a). The moorings were retrieved after a full year of sampling from October 2012 to November 2013 (RV *Pelagia* cruise 64PE 378; Stuut et al. 2013). Initially, each mooring was equipped with two sediment traps at 1200 m (upper, U) and 3500 m (lower, L) water depth. However, the upper sediment trap at Sta. M5 was lost during recovery, so that our dataset is based on all material from the upper and lower sediment traps at Sta. M4 and the lower trap at sampling site M5. Technicap

PPS 5/2 sediment traps were used with a baffled collecting area of 1 m^2 and a rotating carousel with 24 sampling bottles. Prior to deployment, sample cups were filled seawater collected at the deployment site, mixed with HgCl_2 to fix the sample, and buffered with borax, i.e., $\text{Na}_2[\text{B}_4\text{O}_5(\text{OH})_4](\text{H}_2\text{O})_{10}$, to a density in excess of the ambient seawater to prevent the sample from diffusion out of the bottle. Both additives had an end concentration of 1.3 g L^{-1} in the sampling bottle. All sediment traps were programmed for synchronous collection intervals (16 d), starting on October 19 of 2012 and ending on November 7 of 2013. After recovery, the pH and nutrient concentration of the supernatant water were determined, and the sample bottles were stored dark and cool at 4°C until further processing. Tilt meters showed that sediment traps at site M4 remained well within 1.4° from the vertical and at a constant depth during the entire sampling period. At site M5, a downward movement and a tilt up to 14° was recorded during three sampling intervals (intervals #8, 10, and 11), affecting the total mass flux at this site, which was

Table 1. Details regarding the sediment trap moorings. Samples were collected simultaneously and synchronously at all traps from 19 Oct 2012 until 07 Nov 2013 (384 d). mbsl, meter below sea level; MAR, mid-Atlantic ridge.

	Position	Water depth (m)	Trap depth (mbsl)	Closest horizontal distance to seafloor at trap depth (km)
M4U	12.06°N ,	4670	1130	1170
M4U	49.19°W		3370	580 (MAR)
M5L	12.02°N	4400	3520	63
	57.04°W			

corrected accordingly (Gardner, 1985). For further details see Korte et al. (2017).

Water profiling

At each mooring site, CTD profiling and in situ seawater sampling were performed using a Sea-Bird SBE911-Plus Profiler, equipped with sensors for conductivity, temperature, pressure, oxygen, fluorescence, and turbidity during the RV *Pelagia* cruise 64PE 378 in late 2013 (Stuut et al. 2013). The CTD profiler was deployed in conjunction with a SBE32 (24-position) Multi Water Sampler (Rosette), collecting water at pre-defined depths during the upward cast for nutrient analysis. Inorganic nutrient concentrations were determined colorimetrically for phosphate, silicate and nitrate (Murphy and Riley 1962; Strickland and Parsons 1972; Grasshoff et al. 1983) using a Seal-Analytical QuAatro Autoanalyzer connected to an auto-sampler. In addition, Argo float water profiles (<http://www.argo.net/>) were used to investigate temperature and salinity variations around the trap locations ($2^\circ \times 2^\circ$ latitude–longitude box centered around each trap location) during the entire sampling. The profiles were visualized by Ocean Data View (Schlitzer 2018, Data S1) and the seasonal mixed layer (SML) was derived by depth determination at which temperature, salinity, and potential salinity deviated noticeably from their equal values at the surface.

Satellite data

Satellite-derived atmospheric and oceanographic parameters were retrieved for the sediment trapping period and used as complementary information to evaluate the environmental conditions during which the particle export fluxes occurred. The satellite data included aerosol optical depth (AOD) as an indicator for atmospheric dust concentrations, precipitation, sea surface temperature (SST) and salinity (SSS), as well as surface Chl *a* concentrations and the euphotic depth. The data were retrieved for a $2^\circ \times 2^\circ$ latitude-longitude box around each trap location. For source details and additional method information see also Guerreiro et al. (2017). In addition, monthly surface Chl *a* concentrations from October 2013 to December 2013 were retrieved for the broader area in the WTNA (45° – 60° W, 15° N– 5° S) and visualized using Ocean Data View (Schlitzer 2018) for tracking the seasonal dispersal of the Amazon River plume.

In order to investigate the effects from eddy- and wind-driven upwelling in this region, progressive SSS, sea level anomalies (SLA) and the Ekman Vertical Velocity were animated for an area covering a $26^\circ \times 20^\circ$ latitude–longitude box from 38° to 64° W and 16° N to 4° S (Data S1). SLA are typically used for identifying and tracking eddies since this variable account only for the anomaly flow associated with the ring-like features (e.g., Faghmous et al. 2015). The relatively stronger mean flow signal, which could potentially mask the eddies, is excluded from the SLA. Due to the geostrophic balance, anticyclonic eddies are characterized by downwelling and deepening of the thermocline, while cyclonic eddies are

marked by upwelling and raising of the thermocline. Although high biological productivity is often associated with cyclonic eddies, anticyclonic eddies also have the potential to trigger high productivity by, for instance, trapping and transporting nutrient-rich waters (Dufois et al. 2016).

Sediment trap material analysis

The sediment trap material was analyzed for bulk particle composition and mass flux (Korte et al. 2017), as well as for lithogenic (Van der Does et al. 2016; van der Does et al. 2018a,b) and ecological analysis (Guerreiro et al. 2017, 2019). Prior to that, each sediment trap sample was wet-sieved through a 1 mm mesh and subsequently wet-split with a WSD-10 rotary splitter into four 1/5 and five 1/25 subsamples. Subsamples were washed and centrifuged, freeze dried and ground. Total mass was determined by weighing two freeze-dried 1/5 aliquots of each sample, resulting in an average deviation of 1.96% by mass between paired splits of M4 and M5.

One 1/5 split was used for total nitrogen (N_{tot}), total carbon (C_{tot}), and organic carbon (C_{org}) flux analysis, together with their isotope ratios $^{15}\text{N}/^{14}\text{N}$ ($\delta^{15}\text{N}_{\text{tot}}$) and $^{13}\text{C}/^{12}\text{C}$ ($\delta^{13}\text{C}_{\text{org}}$). These data were obtained by combustion with a Thermo Scientific Flash 2000 Elemental Analyzer coupled to a Thermo Scientific Delta V Advantage isotope ratio mass spectrometer. Samples for C_{org} measurements were decalcified with 2 N HCl, while samples for N_{tot} and C_{tot} measurements remained untreated. Carbonate carbon (C_{carb}), mostly produced by calcifying plankton, was calculated as the difference of C_{tot} and C_{org} . Isotope ratios were expressed in standard δ -notation relative to Pee Dee Belemnite (v PDB) for $\delta^{13}\text{C}$ and atmospheric N_2 for $\delta^{15}\text{N}$ via laboratory standards calibrated to international certified reference standards. Sample reproducibility is $\pm 0.01\%$ for N_{tot} , $\pm 0.24\%$ for C_{org} , $< 0.3\text{‰}$ for $\delta^{15}\text{N}_{\text{tot}}$, and $< 0.2 \text{‰}$ for $\delta^{13}\text{C}_{\text{org}}$ values.

The biogenic silica (BSi) flux was analyzed on a different 1/5 split using a sequential-leaching technique with 0.5 M NaOH as a dissolving agent (Koning et al. 2002). Samples were analyzed on a HITACHI U-1100 spectrophotometer and the results were evaluated with a weekly-measured standard calibration curve ($R^2 > 0.99$) resulting in a sample reproducibility of $\pm 0.36\%$.

From all the obtained fluxes, molar C/N ratios as well as the molar rain ratios of $\text{BSi}/C_{\text{carb}}$ and $C_{\text{org}}/C_{\text{carb}}$ were calculated for the individual sampling cups. In addition, total mass flux annual averages were calculated for molar C/N, molar $C_{\text{org}}/C_{\text{carb}}$ and molar $\text{BSi}/C_{\text{carb}}$.

Lithogenic mass $> 0.4 \mu\text{m}$ was determined from one 1/25 split after removal of carbonates, opal and organic matter fractions using the processing protocol for lithogenic minerals (McGregor et al. 2009; Van der Does et al. 2016), followed by filtration of the residue on pre-weighed polycarbonate filters ($0.4 \mu\text{m}$) (Van der Does et al. 2020).

Phytoplankton pigment composition within the sediment trap samples was analyzed on another 1/25 split from the upper trap at site M4 (M4U), using an Ultra-Performance

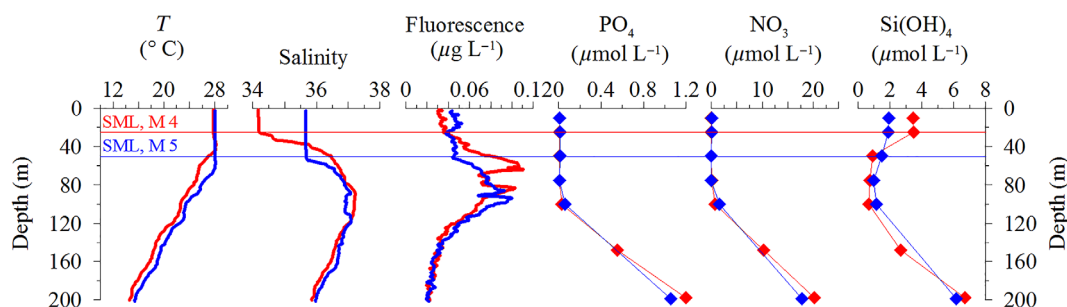


Fig. 2. CTD and nutrient profiles for the upper 200 m at site M4 on November 28th, 2013 (red) and at site M5 on December 1st, 2013 (blue).

Liquid Chromatograph (UPLC) according to the gradient method of Kraay et al. (1992). Each sample was washed with filtered seawater from the original sampling depth (i.e., 1200 m), centrifuged, freeze dried and ground. Pigments in freeze-dried samples were extracted in 95% methanol and centrifuged. Subsequently, the supernatant was filtered (0.2 μm) and 50 μL of sample was injected. The UPLC used was a Waters Acquity system, composed of a 600E controller, a 996-photodiode array in line with a 470 Fluorescence detector. Pigments and degradation products were identified by their absorption spectrum, fluorescence, and elution time, and subsequently converted into concentrations using conversion factors determined with internal standards.

Results

Water column structure

In situ temperature, salinity, and fluorescence measured by CTD at the mooring locations in November and December 2013, indicate that the surface mixed layer (SML) extended down to 25 m depth at site M4 and to ~ 50 m at site M5 (Fig. 2). While surface mixed layer temperature was similar at both sites ($> 27^\circ\text{C}$), salinity was significantly lower at site M4 (34.1) than at site M5 (35.6), indicating freshwater influence from the Amazon River in the open WTNA. Fluorescence depth profiles showed two deep Chl *a* concentrations maxima (DCM) at 60 and 85 m depth at site M4, as opposed to a single DCM at 96 m at site M5. At both sites phosphate and nitrate concentrations were strongly depleted to nearly $0 \mu\text{mol L}^{-1}$ in the surface layers but gradually increasing below the DCM from 100 m. Silicate concentrations were elevated to around $3.5 \mu\text{mol L}^{-1}$ in the freshwater lens occupying the uppermost 25 m at site M4, but much lower ($1.9 \mu\text{mol L}^{-1}$) at site M5.

During the deployment period of the sediment traps, the Argo-float data around site M4 showed SML temperatures ranging between 26°C and 29°C and salinities ranging between 36.95 and 33.97. The SML was deeper during spring compared to fall and winter (Data S1). Greatest deepening of the SML down to 92 m occurred on the 23rd April 2013 in this region (Fig. 3). Surface salinities decreased rapidly in late October to a minimum of 33.97 on the 02 November 2013 (Data S1) similar to the low salinities in the freshwater lens

measured by the CTD in late November 2013 during the recovery of the sediment traps. Argo-float data around mooring M5 were very sparse with only two continuous profiles during June 2013. During this time surface temperature was 28°C and surface salinity ranged between 34.3 and 34.7 (data not shown).

Satellite data

Sites M4 and M5

The satellite data showed similar temporal patterns in AOD around sites M4 and M5 (Fig. 4a,b). AOD increased from low values during the fall 2012 to high values during the summer 2013, after which AOD decreased again in the following fall. At M4, a slight increase relative to fall “background” values was observed in October 2013. Precipitation occurred mainly during summer and fall and more frequently throughout the year at site M5 (Fig. 4c,d). Maximum daily averages amounted to 9 mm in October 2013 at site M4 and to 7 mm in the end of June at site M5. The SSTs showed a similar seasonal trend at sites M4 and M5, with temperatures ranging between 26.2°C and 29.2°C at site M4 and between 26.7°C and 30.1°C at site M5 (Fig. 4c,d). Highest temperatures occurred in the fall while the lowest temperatures were recorded from late

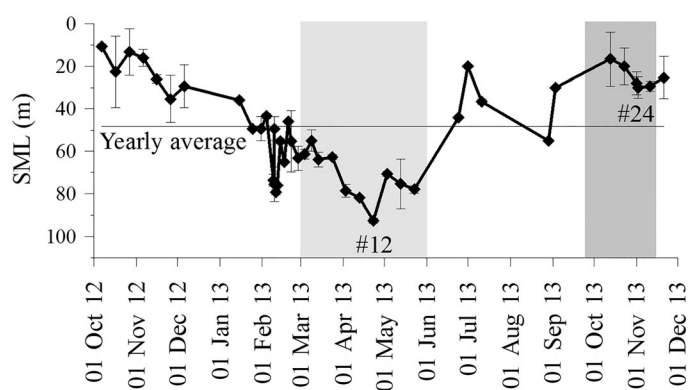


Fig. 3. Depth of the seasonal mixed layer (SML) interpreted from the depth at which temperature, salinity, and potential salinity deviated noticeably from their equal values of the surface, based on Argo float profiles around site M4 (S1).

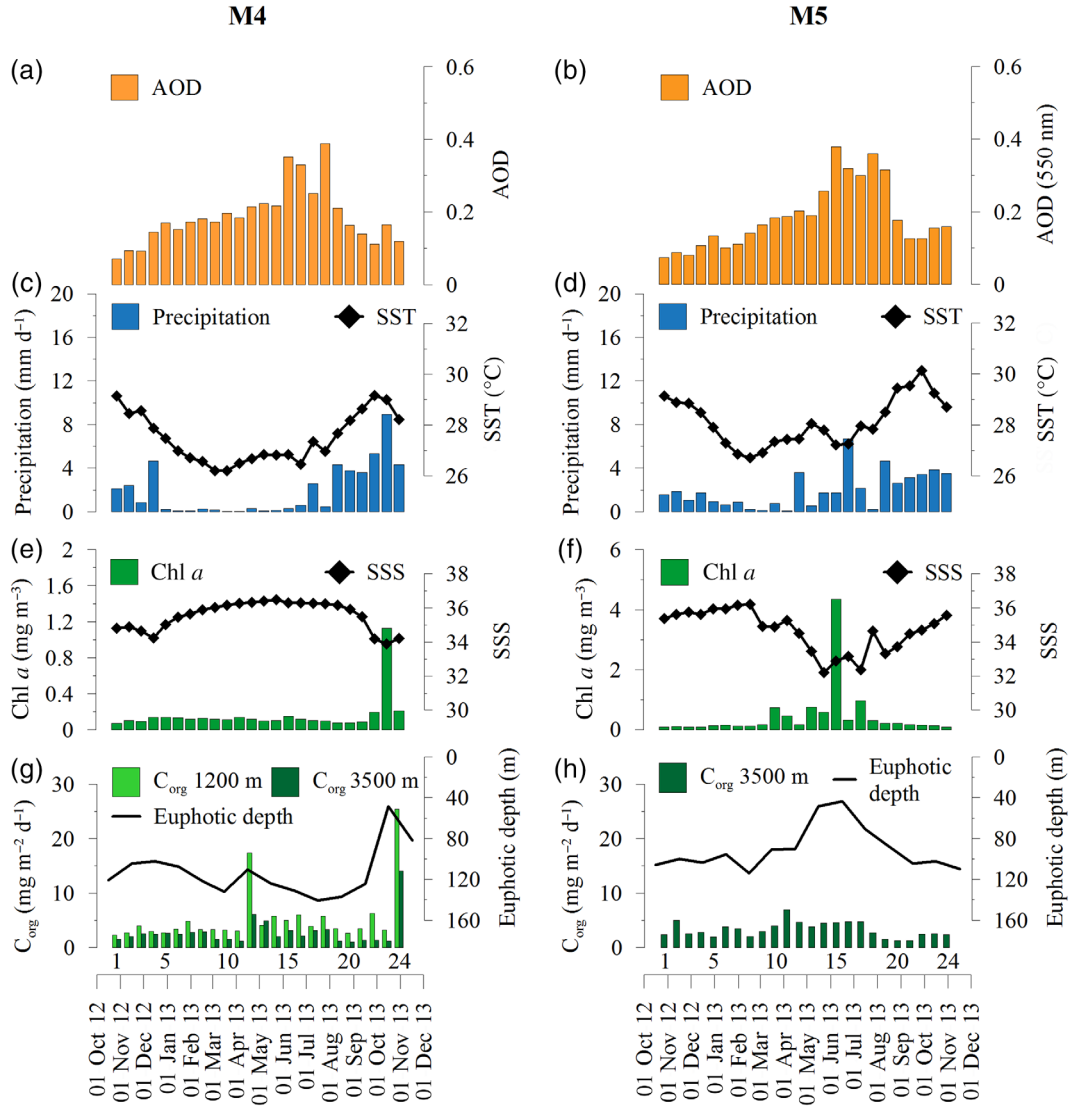


Fig. 4. Satellite-derived data for site M4 (left, see also Guerreiro et al. 2017) and site M5 (right). Parameters from top to bottom are (a,b) aerosol optical depth (AOD), (c,d) precipitation and Sea Surface Temperature (SST), (e,f) Chl *a* concentrations (note different scale for site M5) and Sea Surface Salinity (SSS), (g,h) organic carbon fluxes (Korte et al. 2017) and euphotic depth. Numbers 1–24 indicate the sediment trap sampling intervals.

winter to early spring. Surface Chl *a* concentrations differed substantially amongst the two sampling sites (Fig. 4e,f). Site M4 was marked by low Chl *a* concentrations of $\sim 0.1 \text{ mg m}^{-3}$ throughout the year, except in early October 2013 when values peaked to $> 1 \text{ mg m}^{-3}$ at their maximum absorption (Fig. 4e). At site M5, low Chl *a* concentrations of 0.1 mg m^{-3} were recorded in winter and fall, contrasting with much higher values of $> 4 \text{ mg m}^{-3}$ during spring and summer (Fig. 4f). The SSS showed pronounced minima coinciding with maxima in surface Chl *a* concentrations at both sites (Fig. 4e,f). At site M4, a minimum SSS of 33.8 was reached in October 2013, while at site M5 two minima down to 31.9 were recorded in summer, bracketing the

maximum in surface Chl *a* concentrations. On average, the euphotic depth was deeper and more stable at site M4 compared to M5 (Fig. 4g,h). At M4, the euphotic depth was generally $> 100 \text{ m}$ during most of the year but shoaled to around 50 m in October 2013 when the peak in surface Chl *a* concentration occurred. The euphotic depth also moved upwards during spring, coinciding with the spring peak flux of organic carbon in the upper trap at M4 but remained below 100 m . At site M5, the euphotic depth was around 100 m in fall and winter but shoaled to around 46 m in the summer (Fig. 4h). The shallower euphotic depths were often accompanied by maxima in Chl *a* concentration and simultaneous with minima in SSS.

WTNA

The spatiotemporal variation of surface Chl *a* concentrations, SSS, and to some extent the euphotic depth around the sediment trap mooring locations can be linked to the Amazon River outflow in the WTNA. Combined, the SSS and absolute geostrophic velocity highlight the Amazon River freshwater being dispersed by the surface currents (animation in Data S1.1), whereas the monthly Chl *a* concentrations (October 2012–December 2013) illustrate the progression of the plume after discharge near at the equator at 50°W (Fig. 5). In the first half of

the sampling year, from October 2012 until April 2013, the Amazon River outflow was transported northwestward within the NBC flowing along the northeastern South American coast. During the second half of the sampling year, from May 2013 onwards, the plume became increasingly entrained eastwards into the NECC. Moreover, freshwater (Data S1.1) and large patches of high Chl *a* concentrations (Fig. 5) were seen meandering towards the northwest and crossing the sediment trap sites M5 and M4 during this period, resulting in elevated Chl *a* concentrations, low SSS, and shallow euphotic depths

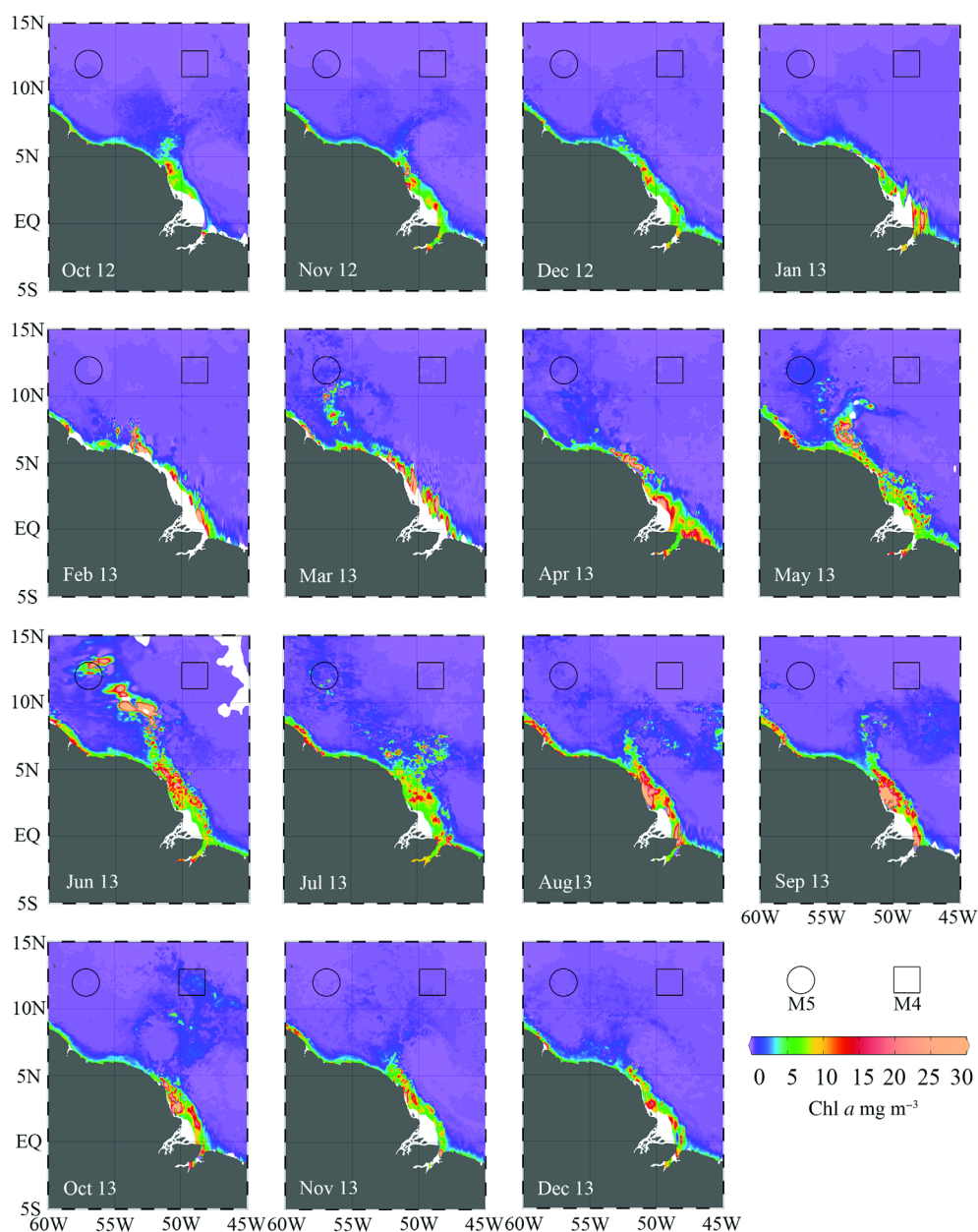


Fig. 5. Monthly Chl *a* concentrations in the surface waters of the WTNA where mooring sites M4 (square) and M5 (circle) were located. The delta of the Amazon River is located at the equator at 50°W. Data obtained from MODIS, Aqua (monthly temporal resolution, 4 km spatial resolution), downloaded from Giovanni of the Goddard Earth Sciences Data and Information Services Center (GES DISC) provided by NASA (disc.sci.gsfc.nasa.gov/).

observed in June at M5 and in October at M4 (Fig. 4e,f). The visualization of SLAs overlapped with their respective anomaly of geostrophic velocity, revealed potential eddy-driven up- and downwelling in the WTNA (animation in Data S1.2). At M5, strong anticyclonic eddies indicative for downwelling were

observed in summer, especially in June 2013. At M4, such eddies were generally less intense except in mid-April (18th–24th) when an anticyclonic eddy was observed promoting downwelling conditions that may have resulted in the shallowing of the euphotic depth in this area (Fig. 4g). The

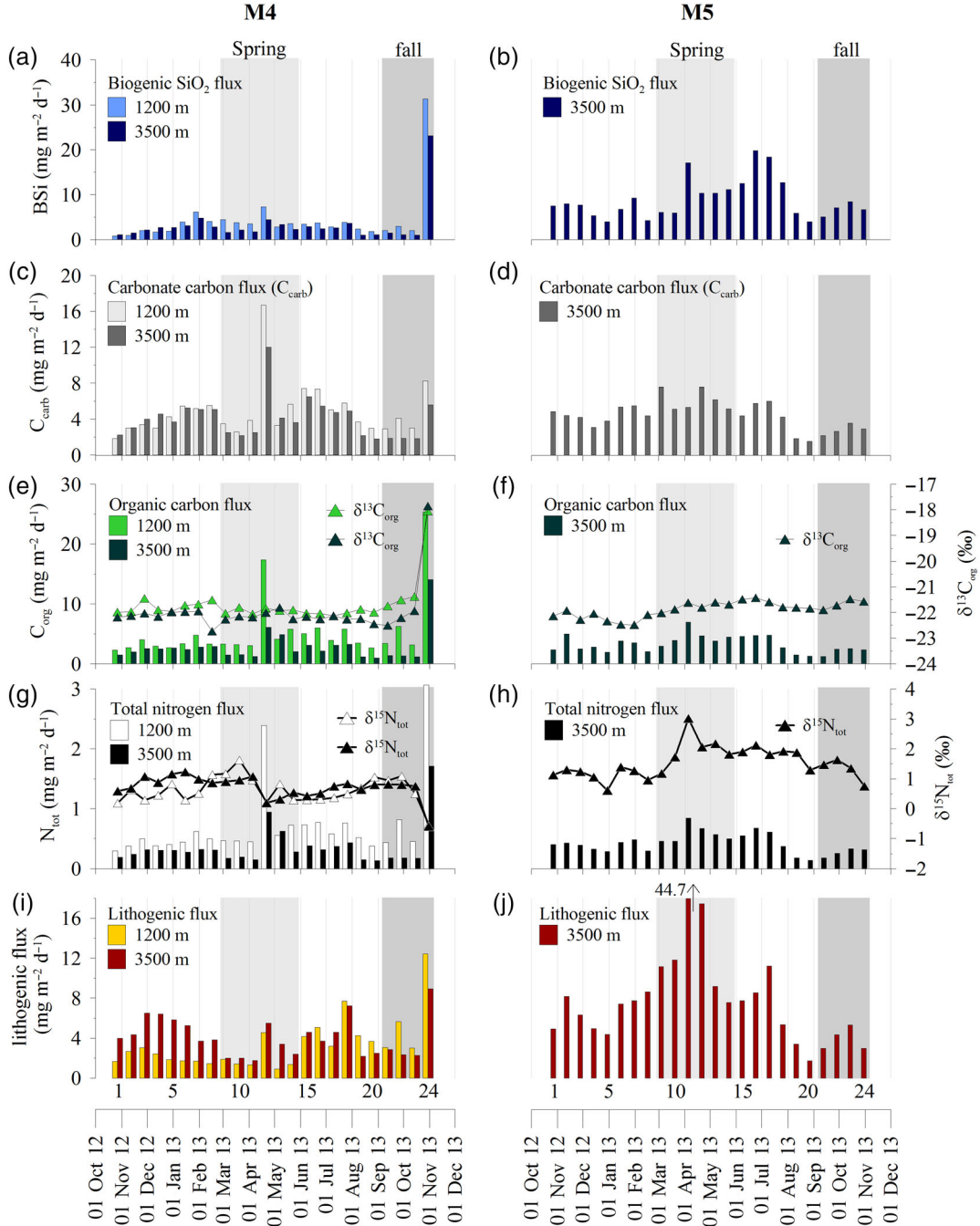


Fig. 6. Particle fluxes and isotopic composition at sites M4 (left) and M5 (right). Mass fluxes ($\text{mg m}^{-2} \text{d}^{-1}$) are shown as bars (left y axis), and isotopic values are displayed in triangles (right y axis in ‰). (a, b) biogenic silica; (c, d) carbonate carbon; (e, f) organic carbon and respective isotope composition; (g, h) total nitrogen and respective isotope composition; (i, j) lithogenic mass flux (Van der Does 2020)

Ekman Vertical Velocities were variable but generally weak over the entire sampling period (animation in Data S1.3), resulting in little large-scale variation in terms of vertical velocities.

Sediment trap material collected at M4 and M5

Particle export fluxes

Mass fluxes at site M4 were higher in the upper sediment trap at 1200 m when compared to the lower sediment trap at 3500 m (Fig. 6, left). While total mass fluxes amounted to $30.9 \text{ g m}^{-2} \text{ yr}^{-1}$ in the upper, they amounted to $23.2 \text{ g m}^{-2} \text{ yr}^{-1}$ in the lower trap, both were marked by weak seasonality (Korte et al. 2017). Peak fluxes were detected simultaneously at both trap depths during spring, in the second half of April 2013, and during fall, in late October/early November 2013.

The two peak flux events differed in composition, they dominated by biogenic silica (BSi) in the fall (Fig. 6a), and by carbonate carbon in spring (Fig. 6b) (Guerreiro et al. 2017; Korte et al. 2017). During the fall event, BSi fluxes exceeded $30 \text{ mg m}^{-2} \text{ d}^{-1}$ (11% of the total mass) in M4U and reaching up to $23 \text{ mg m}^{-2} \text{ d}^{-1}$ (14%) in M4L, while during the rest of the year BSi fluxes ranged from 0.8 to $7.3 \text{ mg m}^{-2} \text{ d}^{-1}$ in M4U, and between 1.1 and $4.8 \text{ mg m}^{-2} \text{ d}^{-1}$ in M4L, with an annual average of 3.1 and $2.3 \text{ mg m}^{-2} \text{ d}^{-1}$, respectively. During the spring peak, carbonate carbon increased to 17 and $12 \text{ mg m}^{-2} \text{ d}^{-1}$ in the M4U and M4L, while annual averages amounted to 5 and $4 \text{ mg m}^{-2} \text{ d}^{-1}$, respectively (Fig. 6c). Organic carbon fluxes varied between 2 – $25 \text{ mg m}^{-2} \text{ d}^{-1}$ for M4U and 1 – $14 \text{ mg m}^{-2} \text{ d}^{-1}$ for M4L, with annual averages of

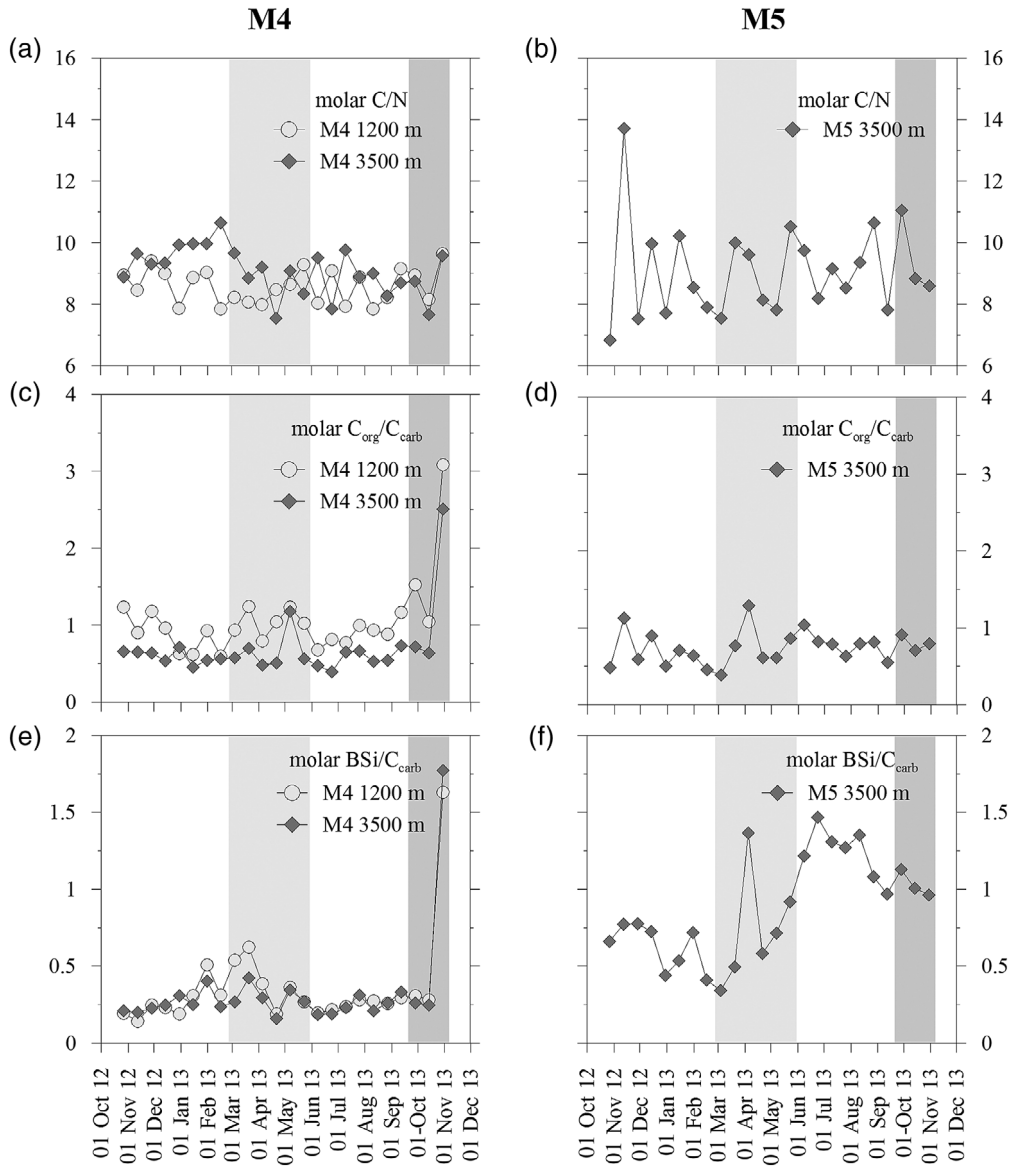


Fig. 7. Rain ratios at site M4 (left) and M5 (right): (a, b) molar C/N ratios; (c, d) molar C_{org}/C_{carb} rain ratio; (e, f) molar BSi/C_{carb} rain ratio.

5.3 and 2.8 mg m⁻² d⁻¹, respectively (Fig. 6e). The total nitrogen showed the same pattern as the organic carbon with fluxes varying between 0.3 and 3 mg m⁻² d⁻¹ for M4U and 0.1 and 1.7 mg m⁻² d⁻¹ for M4L, with an annual average of 0.7 and 0.4 mg m⁻² d⁻¹, respectively (Fig. 6g). Peak fluxes in organic carbon and total nitrogen occurred in tandem with both peaks in total mass flux in spring and fall 2013. The lithogenic fluxes ranged between 1–12 mg m⁻² d⁻¹ in M4U and 2–9 mg m⁻² d⁻¹ in M4L, with annual averages of 3.3 and 4.1 mg m⁻² d⁻¹, respectively (Fig. 6i). Lithogenic fluxes were generally higher during summer at M4U, but showed significant peaks in spring and fall 2013, coinciding with the times of enhanced biogenic fluxes.

At site M5L (3500 m water depth) the annual total mass flux of 42.2 g m⁻² yr⁻¹ was almost two times higher when compared to site M4L at the same depth (Fig. 6, right; Korte et al. 2017). Fluxes of biogenic silica and lithogenic particles increased relative to the fluxes of total nitrogen, carbonate carbon and organic carbon, compared to M4L. High fluxes of 4–20 mg m⁻² d⁻¹ (annual average 9 mg m⁻² d⁻¹) were found for biogenic silica (Fig. 6b) which showed a seasonality with a higher contribution during the summer. Carbonate carbon fluxes varied between 2–8 mg m⁻² d⁻¹ with an annual average of 5 mg m⁻² d⁻¹ (Fig. 6d), while organic carbon varied between 1 and 7 mg m⁻² d⁻¹ with an annual average of 3 mg m⁻² d⁻¹ (Fig. 6f). Total nitrogen fluxes went along with the organic carbon and ranged between 0.1 and 0.8 mg m⁻² d⁻¹ (Fig. 6h). The lithogenic fluxes were much higher compared to M4L, amounting to 2–45 mg m⁻² d⁻¹ (Fig. 6j).

Nitrogen and organic carbon isotope composition

The isotope composition of organic carbon at site M4 ($\delta^{13}\text{C}_{\text{org}}$; Fig. 6e) remained rather constant at around -22‰ in both M4U and M4L, but with slightly more negative values at M4L. However, $\delta^{13}\text{C}_{\text{org}}$ increased by 4‰ to -18‰ at both depths during the peak fluxes of both C_{org} and BSi in fall 2013.

The nitrogen isotope composition at M4U and M4L ($\delta^{15}\text{N}_{\text{tot}}$, Fig. 6g) ranged between -0.6‰ and +1.6‰, with an average of +0.7‰. The drop to -0.6‰ was observed at both depths in the fall, coinciding with the peak flux in nitrogen, organic carbon, the lithogenic fraction and biogenic silica in October–November 2013. The highest $\delta^{15}\text{N}_{\text{tot}}$ value of +1.6‰ was observed at M4U in March 2013.

At site M5L, the $\delta^{13}\text{C}_{\text{org}}$ values were similar to both M4U and M4L, averaging at -22‰, (Fig. 6f). By contrast, the $\delta^{15}\text{N}_{\text{tot}}$ showed more positive values, ranging between +0.6‰ and +3.0‰ and an average of +1.5‰. Highest $\delta^{15}\text{N}_{\text{tot}}$ values of +3.0‰ occurred in April 2013 coinciding with the highest nitrogen fluxes in this trap (Fig. 6h).

Element rain ratios

The molar C/N ratios at site M4 amounted to an annual average of 8.76 at M4U and increased to 9.11 at M4L (Fig. 7a). While molar C/N ratios were rather uniform at M4U, comparatively higher ratios were found during winter at M4L. The

average rain ratios of $\text{C}_{\text{org}}/\text{C}_{\text{carb}}$ amounted to 1.08 at M4U and 0.70 at M4, but ratios in individual sampling cups increased sharply to 3.1 at M4U and 2.5 at M4L in the fall (Fig. 7c). The rain ratios of $\text{BSi}/\text{C}_{\text{carb}}$ were strongly co-variant in M4U and M4L and had similar annual averages of 0.37 and 0.34 throughout the year (Fig. 7e). Again, a significant peak was found in the fall when the ratios increased to 1.7 at both trap depths during the same sampling interval.

Molar C/N ratios at sampling site M5L averaged 9.05, hence similar to the C/N ratio at M4L, but more scattered (Fig. 7b). Annual averages of $\text{C}_{\text{org}}/\text{C}_{\text{carb}}$ amounted to 0.73 with a rather constant value during the year but slightly increasing in early

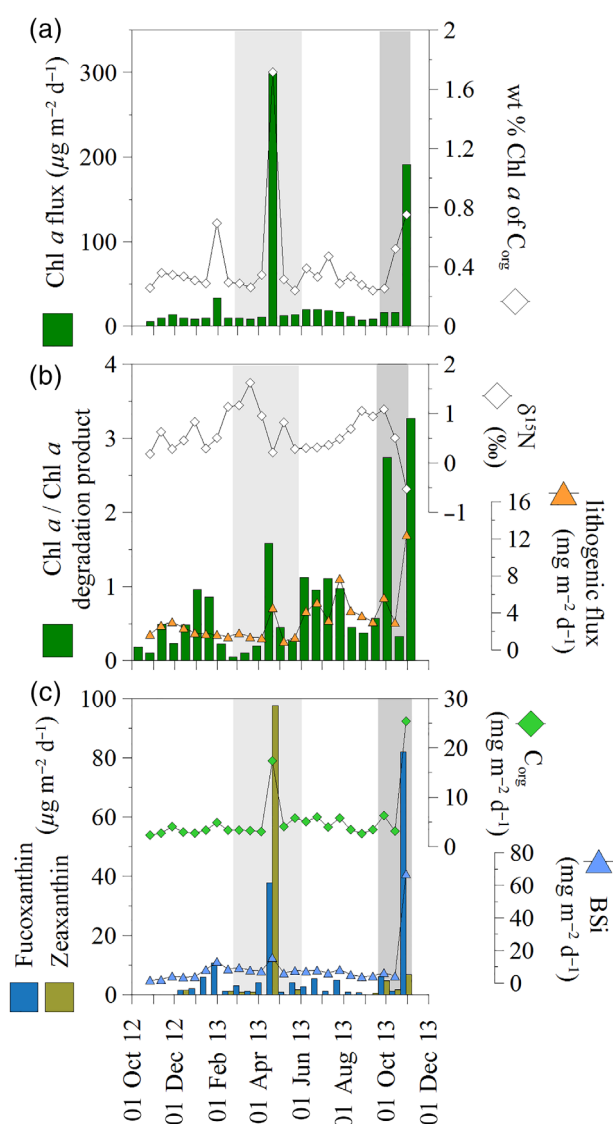


Fig. 8. Phytoplankton pigment content at M4U: (a) fluxes of total Chl *a* (bars) and relative weight % of Chl *a* fluxes to C_{org} (diamonds), (b) Chl *a*/Chl *a* degradation product ratio (bars), $\delta^{15}\text{N}$ values (diamonds) and lithogenic flux (triangles), (c) fluxes of fucoxanthin and zeaxanthin (bars), organic carbon (diamonds) and fluxes of biogenic silica (triangles).

April (Fig. 7d). Molar BSi/ C_{carb} ratios were on average 1.18 but reached higher values in spring and summer when ratios reached 1.5 at their maximum in summer (Fig. 7f).

Phytoplankton pigments

At sampling site M4, the flux of Chl *a* showed two distinct peaks during spring and fall at M4U (Fig. 8a), coinciding with the peak fluxes in C_{org} (Fig. 6g). During the spring of 2013, the Chl *a* peaked at $300 \mu\text{g m}^{-2} \text{d}^{-1}$, equivalent to 1.7 wt% of the organic carbon, whereas during the fall of 2013, it reached almost $200 \mu\text{g m}^{-2} \text{d}^{-1}$ (0.8 wt% of the C_{org}). A third minor Chl *a* peak was observed in winter (January 2013) when Chl *a* amounted to $33 \mu\text{g m}^{-2} \text{d}^{-1}$ (0.7% of C_{org}). The ratio of Chl-*a* to its degradation products pheophorbide and phaeophytin showed several peaks, with highest ratios occurring during spring and fall 2013 (Fig. 8b). In addition, higher ratios were found in summer than in winter. Overall, elevated ratios of Chl *a* to its degradation products were positively correlated with other mass fluxes, including Saharan dust ($r = 0.80$, $p < 0.01$) and weakly negatively correlated with $\delta^{15}\text{N}$ values ($r = -0.54$, $p < 0.05$).

The pigments fucoxanthin and zeaxanthin (Fig. 8c) indicate the community contribution of diatoms and cyanobacteria, respectively (Guillard et al. 1985; Wright and Jeffrey 1987; Barranguet et al. 1997). Fucoxanthin was recorded in almost every sample with values ranging from 8 to $82 \mu\text{g m}^{-2} \text{d}^{-1}$, and highly positively correlated with both organic carbon and biogenic silica ($r = 0.86$ and $r = 0.99$, both $p < 0.01$) and negatively correlated with $\delta^{15}\text{N}$ ($r = -0.61$, $p < 0.01$). Highest values of fucoxanthin were found during spring and fall 2013 in tandem with the peak fluxes in biogenic silica, organic carbon- and carbonate carbon (Fig. 6). Zeaxanthin was only found in low fluxes and discontinuously during the year, but with an exceptionally high peak of nearly $100 \mu\text{g m}^{-2} \text{d}^{-1}$ during spring, when the carbonate flux was also high.

Discussion

Amazon River plume related export productivity

Our most outstanding observations concern the high particle export fluxes that occurred in the fall of 2013 at both sampling depths at site M4, which were each marked by exceptionally high fluxes of biogenic silica, organic carbon, and nitrogen (Fig. 6, Korte et al. 2017). The particle fluxes during this event were exported to the deep sea during the time when the Amazon River plume was being retroflected into the eastward flowing NECC (Muller-Karger et al. 1988). This was evidenced by the presence of a low salinity surface lens and of high Chl *a* concentration patches meandering across the trap location at 12°N and 49°W (Fig. 5, Data S1.1). The sudden increase of Chl *a* concentration to $> 1 \text{ mg m}^{-3}$ in an otherwise oligotrophic ocean region (Fig. 4e) is suggestive of high primary productivity linked to the Amazon River plume. Due to the surface phytoplankton bloom, the water clarity was reduced so that the euphotic depth shoaled from > 100 to

$< 50 \text{ m}$ water depth (Fig. 4g) preventing light penetration to much greater depths (Shipe et al. 2006). Guerreiro et al. (2017) interpreted the occurrence of a pulsed flux maximum in surface-dwelling opportunistic coccolithophore species (i.e., *Gephyrocapsa oceanica* and *Emiliania huxleyi*) as partially reflecting the role of the Amazon River plume in providing nutrients and buoyancy for phytoplankton to bloom at the surface. Indeed, surface salinities as low as 34.1 found in the CTD profile taken 3 weeks after this event, clearly showed the plume in the uppermost 25 m silica-enriched SML (Fig. 2). Earlier studies showed that the increased nutrient availability within the plume changes the composition of phytoplankton into diatom-dominated communities (i.e., *R. clevei* and *Hemiaulus hauckii*) (Shipe et al. 2006; Foster et al. 2007). In the open-ocean, such diatoms often occur in symbiosis with the nitrogen fixating cyanobacteria *R. intracellularis* forming diatom-diazotroph associations (DDAs) (Carpenter et al. 1999; Foster et al. 2007; Subramaniam et al. 2008; Yeung et al. 2012; Goes et al. 2014). This is in good agreement with our trap results, all pointing to the occurrence of DDAs in fall 2013 as well. Firstly, the particle export fluxes at M4 clearly showed an excursion to more negative values of $\delta^{15}\text{N}_{\text{tot}}$ to -0.6‰ (Fig. 6a), indicative for significant contribution by nitrogen-fixers producing biomass with a low $\delta^{15}\text{N}$ between -1‰ and -2‰ (e.g., Bauersachs et al. 2009). Secondly, the $\delta^{13}\text{C}_{\text{org}}$ showed an increase from -22‰ to more positive values of -18‰ (Fig. 6g), showing an enhancement of fast-growing diatoms enriched in ^{13}C compared to other phytoplankton groups (Fry and Wainright 1991). Thirdly, a high amount of fucoxanthin was observed in the sample (Fig. 8c), a pigment that is specific for diatoms (Wright and Jeffrey 1987; Barranguet et al. 1997). These diatoms were ultimately identified as *Rhizosolenia* spp. and *Thalassionema nitzschioides* (Jon Lewis pers. comm.).

DDA blooms have been suggested to represent an important source for new nitrogen in oligotrophic waters (Carpenter et al. 1999) and a sink for CO_2 (Cooley et al. 2007; Subramaniam et al. 2008). This process may be particularly important when the organic matter produced during a phytoplankton bloom is rapidly exported down from the surface to the deep sea (Deuser et al. 1988; Shipe et al. 2006; Chong et al. 2014). The high concentration of Chl *a* we find in combination with the high ratio of Chl *a* to its degradation products (Fig. 8) indicate a fast transport towards the deep with little degradation (Boon and Duineveld 1996). The settling speed was determined to be at least 140 m d^{-1} (Korte et al. 2017) and export fluxes of biogenic silica at M4U and M4L increased to 31 and $23 \text{ mg m}^{-2} \text{d}^{-1}$ when the oligotrophic waters were under the influence of the Amazon River plume in fall 2013. These export fluxes were tenfold, with respect to the averages of $3.1 \text{ mg m}^{-2} \text{d}^{-1}$ and $2.3 \text{ mg m}^{-2} \text{d}^{-1}$ in the upper and lower trap (Fig. 6a), when the Amazon River plume was absent. Similarly, export fluxes of organic carbon also increased around five- to sixfold from an average of 4.5 and $2.3 \text{ mg m}^{-2} \text{d}^{-1}$ to 25 and $14 \text{ mg m}^{-2} \text{d}^{-1}$ (Fig. 6e), testifying to the increased magnitude of the short-

term biological pump. In addition, the significant increase of molar rain ratios in these export fluxes indicate a short but efficient CO_2 sequestration from the sea surface. Under “normal” oligotrophic conditions, $C_{\text{org}}/C_{\text{carb}}$ ratios of 1.3 and 0.6 were found at Demerara station at 13°N , 54°W at 988 and 3755 m water depth, respectively (Honjo et al. 1982; Honjo et al. 2008). Their values are similar to our $C_{\text{org}}/C_{\text{carb}}$ annual averages of 1.1 and 0.7 in the upper and lower trap, respectively (Fig. 7c). However, when impacted by the Amazon River during fall, this ratio increased to 3.1 and 2.5 in the upper and lower trap, respectively. Also, the $\text{BSi}/C_{\text{carb}}$ ratio of 0.3 that Honjo et al. (1982) and Honjo et al. (2008) found at their Demerara station corresponds well to our low $\text{BSi}/C_{\text{carb}}$ ratio of 0.37 and 0.34 in the upper and lower trap (Fig. 7e), but this ratio increased to 1.7 at both trap depths when impacted by Amazon River discharge. The concurrent increase of both the $C_{\text{org}}/C_{\text{carb}}$ and the $\text{BSi}/C_{\text{carb}}$ ratio are a clear and striking departure from average conditions and testify to a proportionally more efficient biological pump during this Amazon driven diatom-dominated event (Berger and Keir 1984; Ittekkot et al. 2000; Rixen et al. 2005).

Assuming that the Amazon-related high fluxes exported at site M4 occurred over the entire distributional range of the river plume (Fig. 5), which can be as large as $\sim 900,000 \text{ km}^2$ (Subramaniam et al. 2008; Chong et al. 2014), one can speculate that the observed organic carbon export fluxes of $25 \text{ mg m}^{-2} \text{ d}^{-1}$ at 1200 m and $14 \text{ mg m}^{-2} \text{ d}^{-1}$ at 3500 m water depth would translate into a sequestration of 0.68 and $0.38 \text{ Tmol C yr}^{-1}$, respectively. In line with observations of organic matter degradation towards the deep ocean (Martin et al. 1987), these values are in agreement with estimates of organic carbon export. Subramaniam et al. (2008) calculated export rates of $2.3 \text{ Tmol C yr}^{-1}$ at 150 m water depth, resulting from diazotrophic fixed carbon and new production based on river nitrate while Chong et al. (2014) found that $\sim 0.15 \text{ Tmol C yr}^{-1}$ is remineralized on the seafloor. Given these export rates the authors concluded that the Amazon River plume provides an important pathway for CO_2

sequestration in the WTNA (Subramaniam et al. 2008) which is higher than in areas that are not influenced by plume waters (Chong et al. 2014). Therefore, our observations add new data supporting the hypothesis that the Amazon River plume acts as an important sink for CO_2 sequestration (Ternon et al. 2000; Cooley et al. 2007; Subramaniam et al. 2008; Yeung et al. 2012). However, they are only rough estimates, hence not allowing us to infer whether the observed surface bloom was equally intense along the entire progression of the Amazon River plume. Still, our observations clearly show high surface productivity linked to the plume being propagated far northeast into the WTNA. These Amazon-related open-ocean blooms appear to be a recurrent feature of the WTNA where site M4 was located, given the high surface Chl *a* concentrations during the fall observed by satellites between 1997 and 2019 (Fig. 9). These surface blooms appear to have occurred approximately every 3–7 years since 1997 over the sampling site M4, and with an increasing frequency in more recent years.

It is currently unknown whether the observed incidence of Chl *a* peaks results from interannual variability in the magnitude of Amazon discharge or from changes in the wind patterns which lead to different and/or stronger ocean surface currents distributing the Amazon discharge. In any case, one might expect that export fluxes linked to these Chl *a* peaks are likely to have, at least on a short-term scale, a significant impact on the CO_2 sequestration in the oligotrophic WTNA.

Unlike site M4, the location of site M5 at 12°N and 57°W (Fig. 1) is more often under the influence of the Amazon River plume when the plume is transported towards the northwest within the NBC (Muller-Karger et al. 1988), or when rings detach from the NBC that subsequently propagate towards Barbados (Fratantoni and Glickson 2001). At M5, the influence of the plume (Fig. 5) resulted in higher particle export fluxes throughout most of the year with highest fluxes observed up to $> 200 \text{ mg m}^{-2} \text{ d}^{-1}$ during spring (Korte et al. 2017). These fluxes are similar to the mass fluxes collected

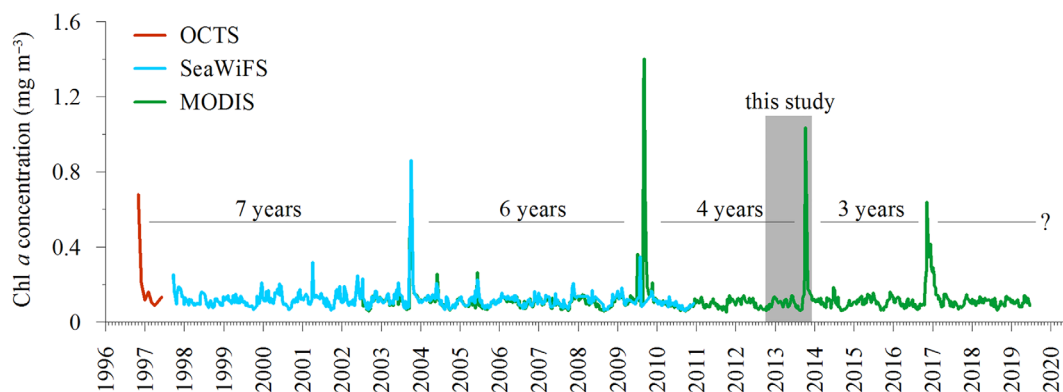


Fig. 9. Satellite derived chlorophyll *a* concentrations at sampling site M4 from November 1997 to June 2019. The satellites used for data retrieval are given in different colors. The period covered by our sediment traps is highlighted in gray.

further north by a sediment trap located 190 km east of Barbados, when the overlying waters were under the influence of the Amazon River plume as well (Deuser et al. 1988).

At site M5 strong anticyclonic eddies passed over the trap location during spring and summer (Data S1.2). These anticyclonic eddies have been reported to be linked to high chlorophyll *a* concentrations, and therefore to be more productive than expected (Dufois et al. 2016). However, the high surface Chl *a* concentrations observed at M5 were not reflected in terms of a striking increase of organic carbon fluxes recorded in the trap at 3500 m (Fig. 4f,h), indicating fast recycling of organic carbon already within the surface waters. As a result, the organic carbon export flux revealed to be quite constant throughout the year with an annual average of $3.3 \text{ mg m}^{-2} \text{ d}^{-1}$ (Figs. 4h, 6f). This amount translates into $0.28 \text{ mmol C m}^{-2} \text{ d}^{-1}$, a value that is within the range of benthic carbon oxidation fluxes ($0.35 \pm 0.18 \text{ mmol m}^{-2} \text{ d}^{-1}$) in the northwestern region of the plume (Chong et al. 2014) where M5 was also located. In addition, our biogenic silica fluxes were also within the range of benthic Si fluxes of $0.25\text{--}0.5 \text{ mmol m}^{-2} \text{ d}^{-1}$ (see fig. 7d in Chong et al. 2014) as our annual average biogenic silica export flux amounted to $9 \text{ mg m}^{-2} \text{ d}^{-1}$ (Fig. 6b), translating into $0.32 \text{ mmol m}^{-2} \text{ d}^{-1}$.

The composition of the exported material, especially the biogenic silica fluxes in relation to carbonate carbon, suggests that the biological pump efficiency was highest in spring and summer when molar $\text{BSi}/\text{C}_{\text{carb}}$ rain ratios were up to 1.5 (Fig. 7f). These ratios are similar to the high $\text{BSi}/\text{C}_{\text{carb}}$ molar rain ratios at M4 during the fall peak. However, as at M4 the biogenic silica flux was most likely dominated by DDAs, the diatom community thriving at M5 may have been different than those at M4. While at M4 the diatoms went along with low $\delta^{15}\text{N}$ values of -0.6‰ , the $\delta^{15}\text{N}$ values at M5 were more positive, reaching up to $+3\text{‰}$ in spring (Fig. 6h). This difference might be related to less nitrogen fixation in the high nutrient, fresher waters close to the Amazon River mouth where coastal diatoms thrive without diazotrophic symbionts (Subramaniam et al. 2008). It might be that these symbiont-free diatoms are less efficient in transferring carbon towards the deep sea compared to the DDAs in more open ocean conditions. The lower efficiency is also expressed in the relatively low $\text{C}_{\text{org}}/\text{C}_{\text{carb}}$ rain ratios at site M5. The ratios remained within the annual average of 0.7 (Fig. 7d) the same value found at M4L and similar to the rain ratio found by Honjo et al. (1982) at their Demerara station.

Export production linked to SML-deepening during spring

Another interesting feature of the WTNA during our sampling year concerns the occurrence of a massive export flux event during the spring of 2013 at site M4, which was enriched in carbonate and organic carbon as well as nitrogen (Fig. 6c,e,g) as well as in phytoplankton pigments (Fig. 8). The same event was marked by a switch in the composition of coccolithophore phytoplankton towards a more opportunistic

species assemblage (i.e., dominated by coccolith fluxes of *Emiliania huxleyi*) concomitant with higher ratios of upper to lower photic zone dwellers, indicating nutrient replenishment and primary productivity in the upper euphotic zone (Guerreiro et al. 2017). Typically, oceanic SSS and low Chl *a* concentrations evidenced by remote sensing observations (Fig. 4e) showed no evidence pointing to any input of nutrient-rich freshwater in this region neither during nor shortly before the event (i.e., between the 13th and 29th April 2013). Rather, our observations suggest that little change occurred in primary productivity at the uppermost part of the ocean. Guerreiro et al. (2017) suggested that the observed change in the coccolithophore assemblages occurred in the subsurface. They ascribe the carbonate rich export flux as an ecological response to nutrient enrichment resulting from dry Saharan dust deposition combined to some degree of wind-forced water mixing during spring. Our SLA observations show an anticyclonic eddy nearing the sampling site around mid-April 2013 (Data S1.2), which could have introduced the required nutrients from below the nutricline which enhanced productivity, as these eddies can trap and transport nutrient-rich waters (Dufois et al. 2016). The anticyclonic eddy pushed the thermocline down and thus deepened the SML, as also evidenced by the Argo float profiles (Fig. 3). The deepening of the SML to around 92 m would have resulted in breaking the nutricline, entraining sufficient nutrients to generate a subsurface bloom in the euphotic zone as suggested by Guerreiro et al. (2017). The subsurface bloom, rich in organic matter, decreased the water clarity and shoaled the euphotic depth (Fig. 4g) but remained undetected from space in terms of elevated chlorophyll concentrations since ocean color sensors only penetrate the upper 5–10 m of the ocean (Marra 2014). Regarding the molar rain ratios during the spring event and therefore its potential for CO_2 sequestration from the surface (Berger and Keir 1984; Ittekkot et al. 2000), it is suggested that this event was less effective as no increase was observed in neither $\text{C}_{\text{org}}/\text{C}_{\text{carb}}$ nor in $\text{BSi}/\text{C}_{\text{carb}}$. The $\text{C}_{\text{org}}/\text{C}_{\text{carb}}$ ratio remained within the yearly average of ~ 1 for, while the $\text{BSi}/\text{C}_{\text{carb}}$ ratio even slightly decreased during this event (Fig. 7).

Particle settling and the influence of Saharan dust

Effective gravitational settling of organic matter from the surface to the deep ocean requires it to be aggregated into larger particles at the surface and ballasted by denser material such as biogenic carbonate and silica, as well as lithogenic particles such as atmospheric mineral dust (Logan and Hunt 1987; Ittekkot 1993; Armstrong et al. 2001; Francois et al. 2002; Klaas and Archer 2002; Fischer and Karakas 2009). First indications of particle aggregation are given by strong correlations between organic carbon fluxes and those of the lithogenic fraction, biogenic carbonate and silica (Data S1). Although this points to interaction between these components, it does not reveal which material is the more important in ballasting. Globally, calcium carbonates are more efficient in ballasting than opaline silica or

lithogenic particles (Francois et al. 2002), but regionally this may be different. The tropical north Atlantic Ocean receives large amounts of Saharan dust (Yu et al. 2015a) and Pabortsava et al. (2017) observed enhanced particle export fluxes, which they linked to Saharan dust deposition in the central North Atlantic gyre as opposed to the South Atlantic gyre where particle export fluxes were lower. For the WTNA, Deuser et al. (1988) suggested that Saharan dust particles contributed to the deep particle flux after deposition in the surface ocean. Their suggestion is confirmed by geochemical analysis of the lithogenic fraction collected by the upper trap at M4, which provided evidence for a northern Africa provenance (van der Does et al. 2018b). In addition, Saharan dust not only acts as ballast material but also as potential nutrient source (e.g., iron, phosphorous) for phytoplankton (Mills et al. 2004), especially when deposited during wet deposition events (Desboeufs et al. 2014; Ridame et al. 2014). This combination also occurred during the fall event at M4, when a drastic flux increase occurred in biogenic silica, organic carbon and Saharan dust (Fig. 6). Elevated AOD values were observed in the fall during times of enhanced precipitation rates (Fig. 4c), and therefore suggest that Saharan dust was delivered via wet deposition and hence having a greater effect on primary productivity via the input of bioavailable nutrients (Desboeufs et al. 2014; Ridame et al. 2014). Consequently, Saharan dust may have provided additional nutrients to those already present in the Amazon River plume. Guerreiro et al. (2017) suggest that the Amazon River plume also acts as retainer for nutrients supplied from the atmosphere. This would indicate that the wet Saharan dust deposition event may have contributed to stimulating nitrogen fixation in the DDA surface bloom. This is in good agreement with the observed low $\delta^{15}\text{N}$ values in tandem with the high lithogenic flux (Fig. 8b). In addition, high lithogenic fluxes go along with elevated Chl *a*/Chl *a* degradation ratios ($r = 0.80$, $p < 0.01$, Fig. 8b), suggesting that Saharan dust might be involved as ballast mineral accelerating particle downward transportation with little organic matter degradation. This is also in accordance with Pabortsava et al. (2017) who attributed low nitrogen isotope ratios to the enhanced particle export fluxes that were linked to Saharan dust deposition. The capacity of Saharan dust deposition to enhance the export of organic matter through increasing its settling velocities, resulting in a up to 10-fold higher particulate organic carbon flux, has been recently confirmed by Van der Jagt et al. (2018).

Conclusions

Particle export fluxes from three sediment traps at two mooring sites in the Western Tropical North Atlantic (WTNA) were combined with satellite data and profiles of the water column from October 2012 to November 2013, to unravel the drivers of the biological pump. Our observations suggest that primary production in the WTNA is stimulated by several processes including Amazon River discharge, nitrogen fixation by marine diazotrophs, seasonal mixed-layer deepening and

Saharan dust deposition. In the oligotrophic region at 49°W, seasonal deepening of mixed-layer led to the introduction of nutrients from below the nutricline in spring 2013, promoting the development of calcifying plankton that triggered a carbonate-rich export peak. This event contrasted with the export peak enriched in biogenic silica that occurred in the fall 2013, when particle fluxes were partially induced by freshwater input from the Amazon River that had been carried as far northeast as 12°N and 49°W by the retroflecting North Brazil Current into the North Equatorial Counter Current. Productivity related to nitrogen fixation and the development of diatom diazotrophic associations is also likely to have contributed to the flux peak recorded in the fall of 2013. In addition, this event might have been stimulated by nutrient input from wet deposition of Saharan dust. Saharan dust and enhanced production of biogenic minerals are likely to have accelerated particle settling, resulting in higher organic carbon export fluxes during this period. While the fall peak at 49°W was most efficient in CO₂ sequestration given the observed high molar rain ratios, fluxes at the westernmost site at 57°W were probably less efficient as indicated by lower organic carbon export fluxes. In conclusion, the WTNA can be a significant sink for CO₂ whenever its oligotrophic waters are fertilized by the Amazon River plume and/or Saharan dust, with the resulting organic particles being rapidly exported, e.g., ballasted, towards the deep ocean with little degradation.

References

- Adams, A. M., J. M. Prospero, and C. Zhang. 2012. CALIPSO-derived three-dimensional structure of aerosol over the Atlantic Basin and adjacent continents. *J. Climate* **25**: 6862–6879. doi:10.1175/JCLI-D-11-00672.1.
- Armstrong, R. A., C. Lee, J. I. Hedges, S. Honjo, and S. G. Wakeham. 2001. A new, mechanistic model for organic carbon fluxes in the ocean based on the quantitative association of POC with ballast minerals. *Deep-Sea Res. II* **49**: 219–236. doi:10.1016/S0967-0645(01)00101-1.
- Barranguet, C., P. Herman, and J. Sinke. 1997. Microphytobenthos biomass and community composition studied by pigment biomarkers: Importance and fate in the carbon cycle of a tidal flat. *J. Sea Res.* **38**: 59–70.
- Basha, G., P. Kishore, M. Venkat Ratnam, T. B. M. J. Ouarda, I. Velicogna, and T. Sutterley. 2015. Vertical and latitudinal variation of the intertropical convergence zone derived using GPS radio occultation measurements. *Remote Sens. Environ.* **163**: 262–269. doi:10.1016/j.rse.2015.03.024.
- Bauersachs, T., and others. 2009. Nitrogen isotopic fractionation associated with growth on dinitrogen gas and nitrate by cyanobacteria. *Limnol. Oceanogr.* **54**: 1403–1411. doi:10.4319/lo.2009.54.4.1403.
- Berger, W. H., and R. S. Keir. 1984. Glacial-Holocene changes in atmospheric CO₂ and the deep-sea record, p. 337–351.

- In J. E. Hansen and T. Takahashi [eds.], Climate processes and climate sensitivity. American Geophysical Union.
- Boon, A. R., and G. C. A. Duineveld. 1996. Phytopigments and fatty acids as molecular markers for the quality of near-bottom particulate organic matter in the North Sea. *J. Sea Res.* **35**: 279–291. doi:[10.1016/S1385-1101\(96\)90755-8](https://doi.org/10.1016/S1385-1101(96)90755-8).
- Bourlès, B., Y. Gouriou, and R. Chuchla. 1999. On the circulation in the upper layer of the western equatorial Atlantic. *J. Geophys. Res.* **104**: 21151–21170. doi:[10.1029/1999JC900058](https://doi.org/10.1029/1999JC900058).
- Carpenter, E. J., J. P. Montoya, J. Burns, M. R. Mulholland, A. Subramaniam, and D. G. Capone. 1999. Extensive bloom of a N₂-fixing diatom/cyanobacterial association in the tropical Atlantic Ocean. *Marine Ecology Progress Series* **185**: 273–283.
- Chong, L. S., W. M. Berelson, J. McManus, D. E. Hammond, N. E. Rollins, and P. L. Yager. 2014. Carbon and biogenic silica export influenced by the Amazon River Plume: Patterns of remineralization in deep-sea sediments. *Deep-Sea Res. I Oceanogr. Res. Pap.* **85**: 124–137. doi:[10.1016/j.dsr.2013.12.007](https://doi.org/10.1016/j.dsr.2013.12.007).
- Cooley, S. R., and P. L. Yager. 2006. Physical and biological contributions to the western tropical North Atlantic Ocean carbon sink formed by the Amazon River plume. *J. Geophys. Res.: Oceans* **111**: 1–14. doi:[10.1029/2006GB002831](https://doi.org/10.1029/2006GB002831).
- Cooley, S., V. Coles, A. Subramaniam, and P. Yager. 2007. Seasonal variations in the Amazon plume-related atmospheric carbon sink. *Global Biogeochem. Cycles* **21**: 1–15. doi:[10.1029/2005jc002954](https://doi.org/10.1029/2005jc002954).
- Desboeufs, K., N. Leblond, T. Wagener, E. B. Nguyen, and C. Guieu. 2014. Chemical fate and settling of mineral dust in surface seawater after atmospheric deposition observed from dust seeding experiments in large mesocosms. *Biogeosciences* **11**: 5581–5594. doi:[10.5194/bg-11-5581-2014](https://doi.org/10.5194/bg-11-5581-2014).
- Deuser, W., F. Muller-Karger, and C. Hemleben. 1988. Temporal variations of particle fluxes in the deep subtropical and tropical North Atlantic: Eulerian versus Lagrangian effects. *J. Geophys. Res.* **93**: 6857–6862. doi:[10.1029/JC093iC06p06857](https://doi.org/10.1029/JC093iC06p06857).
- Duce, R. A., and others. 1991. The atmospheric input of trace species to the world ocean. *Global Biogeochem. Cycles* **5**: 193–259. doi:[10.1029/91GB01778](https://doi.org/10.1029/91GB01778).
- Dufois, F., N. J. Hardman-Mountford, J. Greenwood, A. J. Richardson, M. Feng, and R. J. Matear. 2016. Anticyclonic eddies are more productive than cyclonic eddies in subtropical gyres because of winter mixing. *Sci. Adv.* **2**: 1–6. doi:[10.1126/sciadv.1600282](https://doi.org/10.1126/sciadv.1600282).
- Faghmous, J. H., I. Frenger, Y. Yao, R. Warmka, A. Lindell, and V. Kumar. 2015. A daily global mesoscale ocean eddy dataset from satellite altimetry. *Sci. Data* **2**: 150028. doi:[10.1038/sdata.2015.28](https://doi.org/10.1038/sdata.2015.28).
- Falkowski, P. G. 1997. Evolution of the nitrogen cycle and its influence on the biological sequestration of CO₂ in the ocean. *Nature* **387**: 272–275. doi:[10.1038/387272a0](https://doi.org/10.1038/387272a0).
- Falkowski, P. G., R. T. Barber, and V. Smetacek. 1998. Biogeochemical controls and feedbacks on ocean primary production. *Science* **281**: 200–206. doi:[10.1126/science.281.5374.200](https://doi.org/10.1126/science.281.5374.200).
- Fischer, G., and G. Karakas. 2009. Sinking rates and ballast composition of particles in the Atlantic Ocean: Implications for the organic carbon fluxes to the deep ocean. *Biogeosciences* **6**: 85–102. doi:[10.5194/bg-6-85-2009](https://doi.org/10.5194/bg-6-85-2009).
- Fischer, G., and others. 2007. Mineral ballast and particle settling rates in the coastal upwelling system off NW Africa and the South Atlantic. *Int. J. Earth Sci.* **98**: 281–298. doi:[10.1007/s00531-007-0234-7](https://doi.org/10.1007/s00531-007-0234-7).
- Foster, R. A., A. Subramaniam, C. Mahaffey, E. J. Carpenter, D. G. Capone, and J. P. Zehr. 2007. Influence of the Amazon River plume on distributions of free-living and symbiotic cyanobacteria in the western tropical North Atlantic Ocean. *Limnol. Oceanogr.* **52**: 517–532. doi:[10.4319/lo.2007.52.2.0517](https://doi.org/10.4319/lo.2007.52.2.0517).
- Francois, R., S. Honjo, R. Krishfield, and S. Manganini. 2002. Factors controlling the flux of organic carbon to the bathypelagic zone of the ocean. *Global Biogeochem. Cycles* **16**: 34–31–34–20. doi:[10.1029/2001gb001722](https://doi.org/10.1029/2001gb001722).
- Fratantoni, D. M., and D. A. Glickson. 2001. North Brazil current ring generation and evolution observed with SeaWiFS*. *J. Phys. Oceanogr.* **32**: 1058–1074.
- Fry, B., and S. C. Wainright. 1991. Diatom sources of ¹³C-rich carbon in marine food webs. *Marine Ecol. Progr. Ser.* **76**: 149–157.
- Gao, Y., S.-M. Fan, and J. L. Sarmiento. 2003. Aeolian iron input to the ocean through precipitation scavenging: A modeling perspective and its implication for natural iron fertilization in the ocean. *J. Geophys. Res.* **108**: 1–13.
- Gardner, W.D., 1985. The effect of tilt on sediment trap efficiency. *Deep Sea Research Part A. Oceanographic Research Papers* **32**: 349–361.
- Goes, J. I., and others. 2014. Influence of the Amazon River discharge on the biogeography of phytoplankton communities in the western tropical North Atlantic. *Prog. Oceanogr.* **120**: 29–40. doi:[10.1016/j.pocean.2013.07.010](https://doi.org/10.1016/j.pocean.2013.07.010).
- Grasshoff, K., M. Ehrhardt, and K. Kremling. 1983. Determination of nutrients, p. 159. *In* *Methods of seawater analysis*. Verlag Chemie.
- Guerreiro, C. V., K.-H. Baumann, G.-J. A. Brummer, L. F. Korte, C. Sá, and J.-B. W. Stuut. 2019. Transatlantic gradients in calcifying phytoplankton (coccolithophore) fluxes. *Prog. Oceanogr.* **176**: 102140. doi:[10.1016/j.pocean.2019.102140](https://doi.org/10.1016/j.pocean.2019.102140).
- Guerreiro, C. V., and others. 2017. Coccolithophore fluxes in the open tropical North Atlantic: Influence of thermocline depth, Amazon water, and Saharan dust. *Biogeosciences* **14**: 4577–4599. doi:[10.5194/bg-14-4577-2017](https://doi.org/10.5194/bg-14-4577-2017).
- Guillard, R. R. L., L. S. Murphy, P. Foss, and S. Liaaen-Jensen. 1985. *Synechococcus* spp. as likely zeaxanthin-dominant ultraphytoplankton in the North Atlantic. *Limnol. Oceanogr.* **30**: 412–414. doi:[10.4319/lo.1985.30.2.0412](https://doi.org/10.4319/lo.1985.30.2.0412).

- Gupta, A. 2008. Large rivers: Geomorphology and management. John Wiley & Sons.
- Honjo, S., S. J. Manganini, and J. J. Cole. 1982. Sedimentation of biogenic matter in the deep ocean. *Deep-Sea Res.* **29**: 609–625. doi:10.1016/0198-0149(82)90079-6.
- Honjo, S., S. J. Manganini, R. A. Krishfield, and R. Francois. 2008. Particulate organic carbon fluxes to the ocean interior and factors controlling the biological pump: A synthesis of global sediment trap programs since 1983. *Prog. Oceanogr.* **76**: 217–285. doi:10.1016/j.pocean.2007.11.003.
- Ittekkot, V. 1993. The abiotically driven biological pump in the ocean and short-term fluctuations in atmospheric CO₂ contents. *Global Planet. Change* **8**: 17–25. doi:10.1016/0921-8181(93)90060-2.
- Ittekkot, V., C. Humborg, and P. Schäfer. 2000. Hydrological alterations and marine biogeochemistry: A silicate issue? Silicate retention in reservoirs behind dams affects ecosystem structure in coastal seas. *Bioscience* **50**: 776–782. doi:10.1641/0006-3568(2000)050[0776:HAAMBA]2.0.CO;2.
- Jickells, T. D. 1999. The inputs of dust derived elements to the Sargasso Sea; a synthesis. *Mar. Chem.* **68**: 5–14. doi:10.1016/S0304-4203(99)00061-4.
- Klaas, C., and D. E. Archer. 2002. Association of sinking organic matter with various types of mineral ballast in the deep sea: Implications for the rain ratio. *Global Biogeochem. Cycles* **16**: 63–61–63–14. doi:10.1029/2001gb001765.
- Koning, E., Epping, E., Van Raaphorst, W., 2002. Determining biogenic silica in marine samples by tracking silicate and aluminium concentrations in alkaline leaching solutions. *Aquatic Geochemistry* **8**: 37–67. doi:10.1023/A:1020318610178.
- Korte, L. F., and others. 2017. Downward particle fluxes of biogenic matter and Saharan dust across the equatorial North Atlantic. *Atmos. Chem. Phys.* **17**: 6023–6040. doi:10.5194/acp-17-6023-2017.
- Körtzinger, A. 2003. A significant CO₂ sink in the tropical Atlantic Ocean associated with the Amazon River plume. *Geophys. Res. Lett.* **30**: 1–4. doi:10.1029/2003gl01884.
- Kraay, G. W., M. Zapata, and M. J. W. Veldhuis. 1992. Separation of chlorophylls *c*₁, *c*₂, and *c*₃ of marine phytoplankton by reversed-phase-C18-high-performance liquid chromatography. *J. Phycol.* **28**: 708–712. doi:10.1111/j.0022-3646.1992.00708.x.
- Lefèvre, N., G. Moore, J. Aiken, A. Watson, D. Cooper, and R. Ling. 1998. Variability of pCO₂ in the tropical Atlantic in 1995. *J. Geophys. Res. Oceans* **103**: 5623–5634. doi:10.1029/97jc02303.
- Logan, B. E., and J. R. Hunt. 1987. Advantages to microbes of growth in permeable aggregates in marine systems. *Limnol. Oceanogr.* **32**: 1034–1048. doi:10.4319/lo.1987.32.5.1034.
- Longhurst, A. 1993. Seasonal cooling and blooming in tropical oceans. *Deep-Sea Res. I* **40**: 2145–2165. doi:10.1016/0967-0637(93)90095-K.
- Mahaffey, C., R. G. Williams, G. A. Wolff, N. Mahowald, W. Anderson, and M. Woodward. 2003. Biogeochemical signatures of nitrogen fixation in the eastern North Atlantic. *Geophys. Res. Lett.* **30**: 1–4. doi:10.1029/2002GL016542.
- Marra, J. 2014. Introduction to satellite oceanography. *Limnol. Oceanogr. E-Lectur.* **4**: 1–35. doi:10.4319/lo.2014.jmarra.6.
- Martin, J. H., G. A. Knauer, D. M. Karl, and W. W. Broenkow. 1987. VERTEX: Carbon cycling in the Northeast Pacific. *Deep-Sea Res.* **34**: 267–285. doi:10.1016/0198-0149(87)90086-0.
- Masson, S., and P. Delecluse. 2001. Influence of the Amazon River runoff on the tropical Atlantic. *Phys. Chem. Earth* **26**: 137–142. doi:10.1016/S1464-1909(00)00230-6.
- McGregor, H. V., L. Dupont, J.-B. W. Stuut, and H. Kuhlmann. 2009. Vegetation change, goats, and religion: A 2000-year history of land use in southern Morocco. *Quat. Sci. Rev.* **28**: 1434–1448. doi:10.1016/j.quascirev.2009.02.012.
- Mikaloff Fletcher, S. E., and others. 2007. Inverse estimates of the oceanic sources and sinks of natural CO₂ and the implied oceanic carbon transport. *Global Biogeochem. Cycles* **21**: 1–19. doi:10.1029/2006gb002751.
- Mills, M. M., C. Ridame, M. Davey, J. La Roche, and R. J. Geider. 2004. Iron and phosphorus co-limit nitrogen fixation in the eastern tropical North Atlantic. *Nature* **429**: 292–294. doi:10.1038/nature02550.
- Montoya, J. P., E. J. Carpenter, and D. G. Capone. 2002. Nitrogen fixation and nitrogen isotope abundances in zooplankton of the oligotrophic North Atlantic. *Limnol. Oceanogr.* **47**: 1617–1628. doi:10.4319/lo.2002.47.6.1617.
- Muller-Karger, F. E., C. R. McClain, and P. L. Richardson. 1988. The dispersal of the Amazon's water. *Nature* **333**: 56–59. doi:10.1038/333056a0.
- Murphy, J., and J. P. Riley. 1962. A modified single solution method for the determination of phosphate in natural waters. *Anal. Chim. Acta* **27**: 31–36. doi:10.1016/S0003-2670(00)88444-5.
- Pabortsava, K., and others. 2017. Carbon sequestration in the deep Atlantic enhanced by Saharan dust. *Nat. Geosci.* **10**: 189–194. doi:10.1038/ngeo2899.
- Prospero, J. M. 1999. Long-range transport of mineral dust in the global atmosphere: Impact of African dust on the environment of the southeastern United States. *Proc. Natl. Acad. Sci.* **96**: 3396–3403. doi:10.1073/pnas.96.7.3396.
- Prospero, J. M., E. Bonatti, C. Schubert, and T. N. Carlson. 1970. Dust in the Caribbean atmosphere traced to an African dust storm. *Earth Planet. Sci. Lett.* **9**: 287–293. doi:10.1016/0012-821X(70)90039-7.
- Prospero, J. M., F.-X. Collard, J. Molinie, and A. Jeannot. 2014. Characterizing the annual cycle of African dust transport to the Caribbean Basin and South America and its impact on the environment and air quality. *Global Biogeochem. Cycles* **28**: 757–773. doi:10.1002/2013gb004802.
- Ridame, C., J. Dekaezemacker, C. Guieu, S. Bonnet, S. L'Helguen, and F. Malien. 2014. Contrasted Saharan dust events in LNLC environments: Impact on nutrient dynamics and primary production. *Biogeosciences* **11**: 4783–4800. doi:10.5194/bg-11-4783-2014.

- Rixen, T., M. V. S. Guptha, and V. Ittekkot. 2005. Deep ocean fluxes and their link to surface ocean processes and the biological pump. *Prog. Oceanogr.* **65**: 240–259.
- Schlitzer, R. 2018. Ocean data view, Available from <https://odv.awi.de>.
- Schulz, M., and others. 2012. Atmospheric transport and deposition of mineral dust to the ocean: Implications for research needs. *Environ. Sci. Technol.* **46**: 10390–10404. doi:10.1021/es300073u.
- Shipe, R. F., J. Curtaz, A. Subramaniam, E. J. Carpenter, and D. G. Capone. 2006. Diatom biomass and productivity in oceanic and plume-influenced waters of the western tropical Atlantic Ocean. *Deep-Sea Res. I Oceanogr. Res. Pap.* **53**: 1320–1334. doi:10.1016/j.dsr.2006.05.013.
- Sohm, J. A., E. A. Webb, and D. G. Capone. 2011. Emerging patterns of marine nitrogen fixation. *Nat. Rev. Microbiol.* **9**: 499–508. doi:10.1038/nrmicro2594.
- Strickland, J. D. H., and T. R. Parsons. 1972. A practical handbook of seawater analysis, Supply and Services, Canada.
- Stuut, J.-B. W. and others 2013. Cruise Report RV Pelagia 64PE378, TRAFFIC II: Transatlantic fluxes of Saharan Dust. 9 November–6 December 2013.
- Subramaniam, A., and others. 2008. Amazon River enhances diazotrophy and carbon sequestration in the tropical North Atlantic Ocean. *Proc. Natl. Acad. Sci.* **105**: 10460–10465. doi:10.1073/pnas.0710279105.
- Takahashi, T., and others. 2002. Global sea–air CO₂ flux based on climatological surface ocean pCO₂, and seasonal biological and temperature effects. *Deep-Sea Res. II Top. Stud. Oceanogr.* **49**: 1601–1622. doi:10.1016/S0967-0645(02)00003-6.
- Takahashi, T., and others. 2009. Climatological mean and decadal change in surface ocean pCO₂, and net sea–air CO₂ flux over the global oceans. *Deep-Sea Res. II Top. Stud. Oceanogr.* **56**: 554–577. doi:10.1016/j.dsr.2008.12.009.
- Ternon, J. F., C. Oudot, A. Dessier, and D. Diverres. 2000. A seasonal tropical sink for atmospheric CO₂ in the Atlantic Ocean: The role of the Amazon River discharge. *Mar. Chem.* **68**: 183–201. doi:10.1016/S0304-4203(99)00077-8.
- Van der Does, M., L. F. Korte, C. I. Munday, G. J. A. Brummer, and J. B. W. Stuut. 2016. Particle size traces modern Saharan dust transport and deposition across the equatorial North Atlantic. *Atmos. Chem. Phys.* **16**: 13697–13710. doi:10.5194/acp-16-13697-2016.
- van der Does, M., P. Knippertz, P. Zschenderlein, R. Giles Harrison, and J.-B. W. Stuut. 2018a. The mysterious long-range transport of giant mineral dust particles. *Sci. Adv.* **4**: eaau2768. doi:10.1126/sciadv.aau2768.
- van der Does, M., A. Pourmand, A. Sharifi, and J.-B. W. Stuut. 2018b. North African mineral dust across the tropical Atlantic Ocean: Insights from dust particle size, radiogenic Sr-Nd-Hf isotopes and rare earth elements (REE). *Aeol. Res.* **33**: 106–116. doi:10.1016/j.aeolia.2018.06.001.
- van der Does, M., and others. 2020. Tropical Rains Controlling Deposition of Saharan Dust Across the North Atlantic Ocean. *Geophysical Research Letters* **47**: e2019GL086867. doi:10.1029/2019gl086867.
- Van der Jagt, H., C. Frieze, J.-B. W. Stuut, G. Fischer, and M. H. Iversen. 2018. The ballasting effect of Saharan dust deposition on aggregate dynamics and carbon export: Aggregation, settling, and scavenging potential of marine snow. *Limnol. Oceanogr.* **63**: 1386–1394. doi:10.1002/lno.10779.
- Wright, S., and S. Jeffrey. 1987. Fucoxanthin pigment markers of marine phytoplankton analysed by HPLC and HPTLC. *Marine Ecol. Progr. Ser.* **38**: 259–266.
- Yeung, L. Y., and others. 2012. Impact of diatom-diazotroph associations on carbon export in the Amazon River plume. *Geophys. Res. Lett.* **39**: 1–6. doi:10.1029/2012GL053356.
- Yu, H., and others. 2015a. Quantification of trans-Atlantic dust transport from seven-year (2007–2013) record of CALIPSO lidar measurements. *Remote Sens. Environ.* **159**: 232–249. doi:10.1016/j.rse.2014.12.010.
- Yu, H., and others. 2015b. The fertilizing role of African dust in the Amazon rainforest: A first multiyear assessment based on data from Cloud-Aerosol Lidar and Infrared Pathfinder Satellite Observations. *Geophys. Res. Lett.* **42**: 1984–1991. doi:10.1002/2015GL063040.
- Zhao, T., S. Gong, X. Zhang, and I. McKendry. 2003. Modeled size-segregated wet and dry deposition budgets of soil dust aerosol during ACE-Asia 2001: Implications for trans-Pacific transport. *Journal of Geophysical Resea.* **108**: 1–9. doi:10.1029/2002JD003363.

Acknowledgments

This project is funded by the ERC (project no. 311152) and NWO (project no. 822.01.008). In addition, this study had the support of the European Union, through a Marie Skłodowska-Curie European Fellowship supported by the European Union H2020-MSCA-IF-2017 under grant agreement no. 796802, awarded to Catarina V. Guerreiro (www.dustco-online.pt). The authors acknowledge NIOZ technicians, captains and their crews for their assistance during cruises *Meteor M89* and *Pelagia 64PE378*. The authors thank Jort Ossebaer for helping with the EA-IRMS analysis, Sharyn Ossebaer for assisting with biogenic silica measurements and Evaline van Weerlee for UPLC-measurements. Carolina Sá (MARE, University of Lisbon, Portugal) is thanked for downloading and processing of the satellite data and Jon Lewis (Loughborough University, UK) for diatom identification. The authors would like to thank two anonymous reviewers for their time, comments and helpful suggestions that contributed to improving the manuscript.

Conflict of Interest

None declared.

Submitted 02 July 2019

Revised 03 December 2019

Accepted 15 February 2020

Associate editor: Maria Maldonado